Surface energy balance algorithm for land -based consumption water use of different land uses-cover types in arid-semiarid regions

Shereif H. Mahmoud and A. A. Alazba

ABSTRACT

Spatiotemporal distributions of water consumption for various land use-cover types over the Eastern province of Saudi Arabia were estimated using Surface Energy Balance Algorithm. Water consumption of various land use and cover classes show similar seasonal dynamic trends. The spatial distribution of annual actual evapotranspiration (AET) shows low values in in the Empty Quarter (231–438 mm/yr), and moderate values in the Eastern Province borders (439–731 mm/yr). Very high AET values were observed in irrigated croplands in the Northern plains, Hafar Al-Batin, the central coastal lowlands, and the southern coastal lowlands, where annual AET ranged from 732–1,790 mm/yr, representing the majority of the study area agricultural land. Evaporative behavior of land use-cover types indicated that irrigated cropland which occupies 0.37% of the study area have an average daily AET ranges from 9.2 mm/day in January and a maximum value in April (30 mm/day). Average annual water use by irrigated cropland is relatively very high and it is roughly 1,786.9 mm/yr. While, water bodies, which covers 0.023% (121.2 km^2) of the study area, also had relatively high mean AET (660.8 mm/yr). Overall, AET rates for irrigated cropland are much higher than for other land uses.

Key words | arid-semiarid regions, land uses-cover, surface energy balance algorithm, water consumption, water resource management

Shereif H. Mahmoud (corresponding author)
A. A. Alazba
Alamoudi Water Research Chair,
King Saud University,
P.O. Box 2460,
Riyadh 11451,
Saudi Arabia
E-mail: *eng.shereif1@hotmail.com*

INTRODUCTION

Fundamental information on irrigation practices and groundwater resources is perceived as a missing part for building the water sector strategy of the Kingdom of Saudi Arabia (KSA). Water is declining rapidly in rural and urban areas, generally because of the growth in agricultural requirements (Mahmoud & Alazba 2016). Evapotranspiration (ET) constitutes a major part of the hydrological cycle, and is considered to be a means of exploiting irrigation water (Papadavid *et al.* 2011). For the agricultural production, water is a fundamental component and as well as critical for future global food security. During the past few decades, fast growing world population, urbanization, and industrialization caused depletion of fresh water resources. Agricultural water demand in Saudi Arabia comprised about 83–90% of the total water demands during 1990–2009 (Chowdhury & Al-Zahrani 2015). In order to better assess and manage irrigation water, estimating the amount of water consumed for agriculture-related activity is very important because it is a primary consumer of water. Since a large amount of irrigated water is lost through ET, its accurate estimation can be helpful for efficient management of irrigation water. Improved irrigation water management requires accurate scheduling of irrigations, which in turn requires an accurate calculation of daily ET (Bausch 1995). Determination of AET from remote sensing data is based on the assessment of the surface energy balance components with the support of limited meteorological data (Ayenew 2003). Over the past

doi: 10.2166/ws.2016.077

decades, a large fraction of the of hydrological research activities has been directed at accurately estimating ET rates using various spatial and temporal scales. One of the most significant developments in the area of remote sensing hydrology was the determination of distributed a real, AET from satellite data, based on the energy balance approach (Menenti 1984; Parodi 1993; Bastiaanssen 1995; Bastiaanssen *et al.* 1998a).

The surface energy balance algorithm for land (SEBAL) method (Bastiaanssen 1995) enables the calculation of actual and potential ET during the daytime of the satellite data recording. The method calls for complex procedures and determination of a number of variables from the different spectral bands of the satellite data, such as surface kinetic temperature, Normalized Difference Vegetation Index (NDVI), emissivity and albedo. Bastiaanssen (1995) described the method in detail. The widely adopted SEBAL model was generally utilized in farming areas (Bastiaanssen *et al.* 2005), where the flat landscape minimizes the spatial heterogeneities of the energy fluxes if compared to the effects of morphology on meteorological variables. For these agricultural contexts, numerous applications can be found in the literature (e.g., Bastiaanssen 2000; Minacapilli *et al.* 2009), chiefly focusing on the establishment of model outputs at the platform overpass time via of simultaneous micro-meteorological measurements. Moreover, some applications were carried to regional (e.g., Sánchez *et al.* 2008) or basin (e.g., Teixeira *et al.* 2009) scales, by altering the assessment of instantaneous fluxes to account for the effects of complex morphologies.

In recent years, an increasing number of satellite algorithms based the surface energy balance equation have been developed to estimate actually a real- averaged ET by incorporating remotely sensed variables such as land surface temperature (LST), surface albedo, vegetation cover fraction, and land cover (LC) type in conjunction with a field observations (Bastiaanssen 2000; Boronina *et al.* 2005; Senay *et al.* 2007; Wang *et al.* 2007; Singh *et al.* 2008; Elhaddad *et al.* 2010; Liu *et al.* 2010). Wang *et al.* (2007) proposed a simple regression equation to estimate ET using surface net radiation, air, surface temperatures, vegetation indices and ground-based measurements available at eight enhanced surface facility sites located throughout the Southern Great Plains area of the United States. Their work concluded that AET can be reasonably predicted using a correlation coefficient that varies from 0.84 to 0.95 under a wide range of soil moisture conditions and LC types. More recently, Singh *et al.* (2008) conducted a study to assess the operational characteristics and performing large-scale mapping of spatial distributions and seasonal variation in south-central Nebraska climates. The outcomes of their work showed that the model was capable of predicting growing season cumulative daily corn ET reasonably well within 5% of the measured values and they concluded that SEBAL can be a feasible instrument for generating ETc maps to assess and quantify the spatiotemporal distribution of ET on large scales as well as estimating surface energy fluxes. Elhaddad *et al.* (2010) used the energy balance-based model to estimate the spatial and temporal variability of AET in the Arkansas River Basin in Colorado, South Platte River Basin in Colorado, and Palo Verde Irrigation District in California along with a 1-day ET estimate for the Texas. Another study conducted by Liu *et al.* (2010) to estimate AET and determine the variation with regards to varying types of land use and LC in urban settings. They implemented the SEBAL model to estimate AET at a higher spatial resolution using Landsat 5 satellite images and field observations. Their results revealed that the lowest observed AET was for developed urban areas and the highest for open water bodies. The AET difference is also presented from two contrasting counties. The results also indicated that agricultural fields as having higher AET values than those of urban settings for all LC types except open water bodies.

The SEBAL model has been tested under several irrigation conditions in Egypt, India, Sri Lanka, Pakistan, Afghanistan, Argentina, Turkey, Niger, China, Brazil, United States, Sudan and Spain to diagnose the uniformity in crop consumptive use, crop water stress and irrigation performance (Wang *et al.* 1995; Bastiaanssen *et al.* 1998a, 1998b; Bastiaanssen 2000; Senay *et al.* 2007; Bastiaanssen *et al.* 2012; Wu *et al.* 2015). The first attempt to assess actual irrigation applications based on remotely sensed ET observations was presented by Ramos *et al.* (2006). The authors used SEBAL model to assess the AET and to compute net water volumes and net irrigation volumes by introducing a water application efficiency factor. They reported that it is possible to assess actual irrigation

applications based on AET observations. A similar study was conducted by Senay *et al.* (2007) using a simplified surface energy balance model to monitor and measure the performance of irrigated farming in Afghanistan. They used a combination of 1-km, thermal data and 250- m NDVI data, both from the Moderate Resolution Imaging Spectroradiometer (MODIS) sensor. Seasonal AET over a period of six years for two major irrigated basins were computed by analyzing up to 19 cloud-free thermal and NDVI images from each year. Senay *et al.* (2007) reported that one of the major advantages of the energy-balance approach is that it can be applied to measure the spatial extent of irrigated areas and their water-use dynamics independent of the source of water as opposed to the water balance model that requires knowledge of both the magnitude and temporal distribution of rain and irrigation applied to field.

In the present study, the spatial and temporal distributions of reference and AET over the Eastern province of Saudi Arabia during 1992–2013 were estimated using a surface energy balance based algorithm. The zonal statistics for each sort of land-cover type was also carried out, in order to interpret the water consumptions of different land use-cover types.

MATERIAL AND METHODS

Description of the study area

The Eastern Province (Figure 1) is the largest province of Saudi Arabia and it occupy an area of 518,300 km^2. It borders the Persian Gulf, which contains the province's only maritime boundary and borders five countries on earth. Aside from this watery border, the majority of the states that the Eastern Province borders are on solid ground, and those are Iraq, Kuwait, Oman, Qatar, and the United Arab Emirates. The largely uninhabited Rub' al Khali (Empty Quarter) desert occupies more than half of the region. Geologically, Tertiary sediments characterize the whole district with significant areas covered by eolian sands and late Tertiary to Quaternary gravel sheets. The entire region is divided into eight sub regions. They are Northern plains, the central coastal lowlands, the southern coastal lowlands, northern summan, southern summan, northern Dahna, southern Dahna and the Rub al-Khali. The Northern plain is a linear depression bordering Hafar Al-Batin. It is a large dead, flat plain rising very gradually from sea level in the east to about 400-m elevation in the west. The region

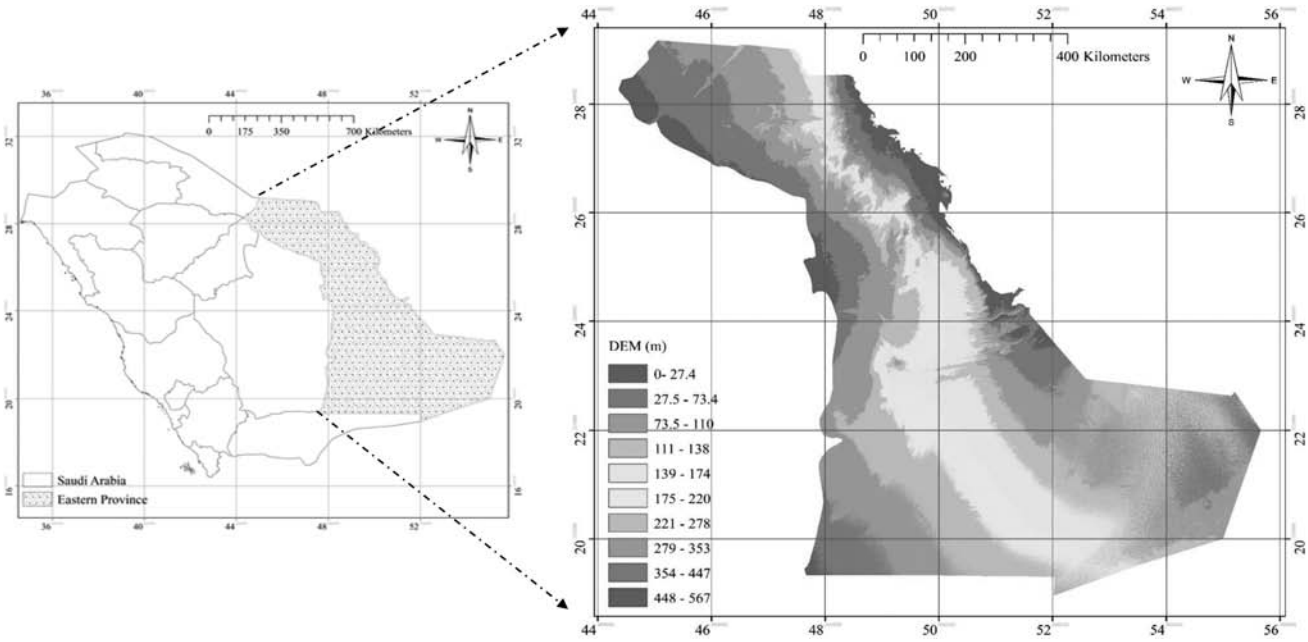

Q4 **Figure 1** | Location map of the study area.

is magnificent in many respects being the largest continuous sand sheet of the world. Some of the sand dunes in this part of the desert is as high as 250 m. Clime of the Eastern Saudi Arabia is mostly arid with temperature rising from 15 °C in January to a maximum of about 42 °C in August-September period. Annual rainfall means range from around 113–275 mm/yr in the north and northwest to less than 30 mm in the Empty Quarter (Figure 2). The vegetation of the Eastern regions is generally sparse. Annual plants, which comprise approximately 60% of the vegetation cover, are dominating in wadis and other shallow depressions.

Reference evapotranspiration

Climatic data obtained from meteorological department, Ministry of Agriculture and Ministry of Water and Electricity. Reference evapotranspiration is the ET from a hypothetical surface. In the case of the United Nations Food and Agriculture Organization (FAO) method (Monteith 1965), this surface consists of a grass reference crop of 0.12-m in height that is actively growing and adequately watered. It should have a surface roughness of 70 (s/m) and an albedo of 0.23. The latent heat flux of this reference surface is estimated according to the Penman–Monteith equation. In this study, 63 years of daily climate data (1992–2013) collected from weather stations located across the study region were utilized. Penman–Monteith method (Monteith 1965) was used for estimating ET_O on a grid-by-grid basis using Equation (1).

$$ET_o = \frac{0.408\Delta(Rn - G) + \gamma \frac{900}{T + 273} u_2 (e_s - e_a)}{\Delta + \gamma(1 + 0.34u_2)} \quad (1)$$

where

ET_o = reference evapotranspiration (mm/day)
Rn = net radiation at the crop surface (mj/m^2/day),
G = soil heat flux density (mj/m^2/day),

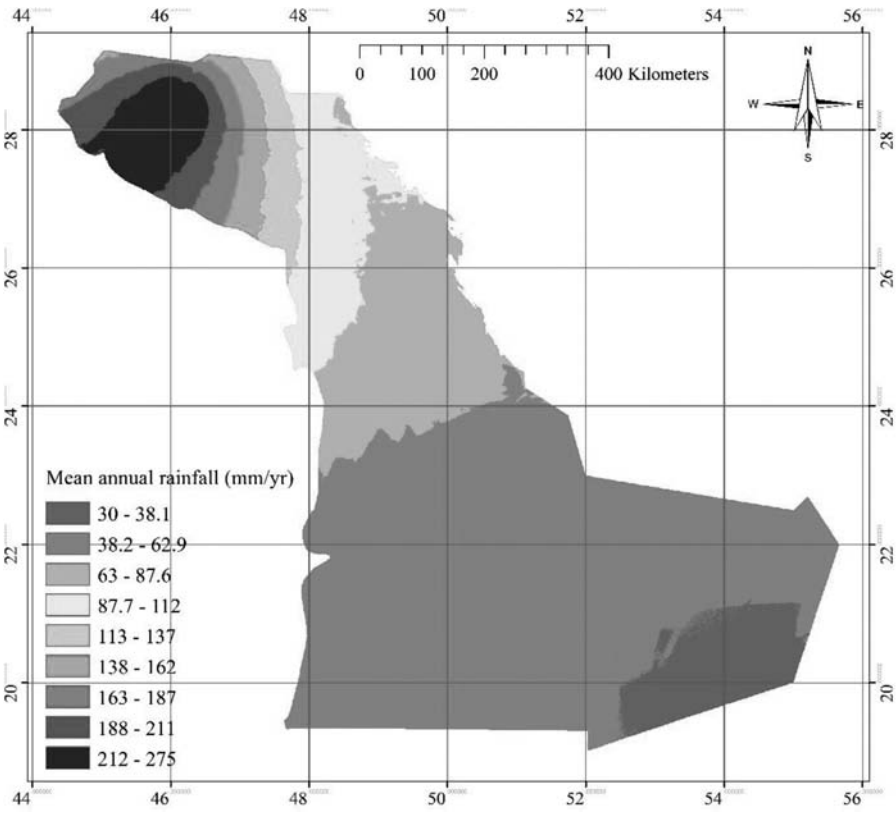

Q5 **Figure 2** | Mean annual rainfall (1992–2013).

T = mean daily air temperature at 2 m height (°C),
u_2 = wind speed at 2 m height (m/s),
e_s = saturation vapour pressure (kPa),
e_a = actual vapor pressure (kPa),
Δ = slope vapor pressure curve (kPa/°C),
γ = psychrometric constant (kPa/°C).
e_s-e_a = saturation vapor pressure deficit (kPa)

The data include elevation, latitude and longitude of the station, total monthly rain, maximum and minimum air temperature, relative humidity, wind speed at 2-m height, and daily sunshine hours. Penman–Montieth calculations were implemented within the main program of GIS. Prior to calculating ET. The inverse distance weighted (IDW) interpolation function was utilized to interpolate the values of the input data for each Julian day throughout the year.

The SEBAL model

Actual evapotranspiration (AET) retrieval, either by means of remote sensing-based approaches or by micro-meteorological measurements, is based on the application of the surface energy balance equation to the soil–plant–atmosphere system. SEBAL is one of the residual methods of energy budget, developed by (Bastiaanssen *et al.* 1998a). It combines empirical and physical parameterization. The remote sensing data used in this study included MODIS atmospheric profile data (MOD07). Near surface temperature values were extracted at the pressure level closest to the ground-surface described by the region's digital elevation model (DEM). Daily data were averaged to generate monthly averages. Data were further improved by relating MODIS-Ts to climate-station temperatures using MODIS LST data (MOD11A2). Emissivity values were derived by averaging MODIS-bands 31 and 32 emissivities, NDVI (MOD13Q1), MODIS products combined with BRDF-albedo products (MCD43B3). Shuttle Radar Topographic Mission DEM (gap-filled) were obtained from the consortium of spatial data and information. The inputs also included local weather data and satellite data. From the input data, the *Rn* (net solar radiation), *NDVI*, albedo, roughness length, and *G* (soil heat flux) were calculated. The Solar Analyst tool in ESRI's ArcGIS-environment was used to model solar radiation (Fu & Rich 1999). This tool is capable of generating both point and area-integrated estimates of solar radiation for variable time intervals. This balance, under the hypothesis that advection, energy required for photosynthesis, and canopy and air storages are negligible, can be written as:

$$\lambda ET_{ins} = R_n - G - H \tag{2}$$

where R_n (W m^{-2}) is the net radiation, G (w/m^2) is the soil heat flux at the surface, H (w/m^2) is the sensible heat flux and λET_{ins} (w/m^2) is the latent heat flux, which represents the energy amount used for the surface evaporation and plant transpiration processes. The instantaneous surface energy balance (Equation (2)), at satellite overpass time is solved for λET_{ins} by applying a residual approach. In the framework of SEBAL modeling, the net radiation, Rn computed based on the balance between downwelling and upwelling shortwave and long-wave radiation: The equation to calculate the net radiation flux is given by

$$Rn = (1-\alpha)Rs_{\downarrow} - Rl_{\downarrow} - Rl_{\uparrow} - (1-\varepsilon_o)Rl_{\downarrow} \tag{3}$$

where Rn is the net radiation at the surface, α is the surface albedo, $Rs_{\downarrow}$ is the incoming short-radiation, $Rl_{\downarrow}$ is the incoming long-wave radiance, $Rl_{\uparrow}$ is the outgoing long-wave radiation, and ε_o is the surface emissivity. Albedo is the ratio of reflected light to total incident sunlight for a given area of the land surface. It is a fundamental property controlling the energy flux at the surface of the Earth; it can provide information on the biophysical characteristics of the land surface including the structure of vegetation canopies, soil moisture, and urbanization. Broadband albedos are calculated using spectral-to-broadband conversion algorithms. The MODIS albedos represent the best quality data possible for each 16-day period (Zhou *et al.* 2003). Wanner *et al.* (1997) provided a detailed description of the MODIS albedo product, its creation, and its validation. These products were developed based on atmospherically corrected, cloud-cleared reflectance observations from the MODIS sensors on NASA's Aqua and Terra satellites.

DEM-based methods to estimate net shortwave radiation prove sound for clear sky conditions (Ruiz-Arias *et al.* 2009). In the present study, we used the Solar Analyst

tool in ESRI's ArcGIS-environment to model solar radiation. The tool is capable of generating both point and area-integrated estimates of solar radiation for variable time intervals.

$$Rs_{\downarrow} = 1,367 \times COS\theta \times d \times \tau_{sw} \tag{4}$$

where, $COS\theta$, is the cosine of the solar incidence angle, d is the inverse squared relative earth-sun distance, and τ_{sw} is the atmospheric transmissivity. The atmospheric transmissivity values were determined based on clear sky and relatively dry conditions obtained using the following elevation-based relationship $\tau_{sw} = 0.75 + 2Z \times 10^{-5}$ (Allen *et al.* 1998), where Z is the elevation of the weather station above sea level (m).

The incoming long-wave radiance $Rl_{\downarrow}$ and the outgoing long-wave radiation $Rl_{\uparrow}$ are derived from an application of the Stefan–Boltzmann equation and MODIS-based T_s and T_a as input, i.e.

$$Rl_{\uparrow} = \varepsilon_o \times \sigma \times T_s^4 \tag{5}$$

$$Rl\downarrow = \varepsilon_a \times \sigma \times T_a^4 \tag{6}$$

where T_s is the mean surface temperature (k), which is obtained from the satellite data. Daily T_s data were averaged to generate monthly averages. Data were further improved by relating MODIS-T_s to climate-station temperatures.

σ is the Stefan Boltzmann constant (5.67×10^{-8} w/m^{2}k^2), ε_o is the broad-band surface emissivity, The surface emissivity was computed using an empirical equation where the NDVI > 0 by inputting the NDVI and the LAI as described in the SEBAL user manual, ε_a is the emissivity of the atmosphere, Emissivity of the atmosphere was calculated from Equation (8).

$$\varepsilon_a = 0.85 \times (-\ln \tau_{sw})^{0.09} \tag{7}$$

Substituting (8) into (7) provides the following Equation (8)

$$Rl\downarrow = 0.85 \times (-\ln \tau_{sw})^{0.09} \times \sigma \times T_a^4 \tag{8}$$

Soil heat flux cannot be directly determined from satellite sensors and requires empirical formulation. Remote sensing derivable parameters that influence soil heat flux are used; these include NDVI, surface temperature and albedo. The soil heat flux (G) has been estimated using the following relation developed by Bastiaanssen (1995):

$$G = \left[\frac{Ts - 273.16}{\alpha}(0.0038\alpha + 0.007\alpha^2)(1 - 0.98NDVI^4)\right] \times Rn \tag{9}$$

Sensible heat flux is the rate of heat loss to the air by convection and conduction, due to a temperature difference. It was computed using the following equation for heat transport:

$$H = \frac{\rho \times c_p \times (T_s - T_a)}{r_{ah}} = \frac{\rho \times c_p \times dT}{r_{ah}} \tag{10}$$

where ρ is the air density (kg/m^3), c_p is the specific heat of air (1,004 j/kg k), dT is the near surface temperature difference (k), and r_{ah} is the aerodynamic resistance to heat transport (s/m), where

$$\Delta T = \left(\frac{dTdry - \Delta Twet}{Tsdry - Tswet}\right) \times Ts - \left(\frac{dTdry - dTwet}{Tsdry - Tswet}\right) \times Tswet \tag{11}$$

The aerodynamic resistance to heat transport (r_{ah}) is computed for neutral stability as:

$$r_{ah} = \frac{\ln(\frac{z_2}{z_1})}{u^* k} \tag{12}$$

where Z_1 is a height just above the zero displacement distance height of the plant canopy set to 0.1 m for each pixel, and Z_2 is the reference height just above the plant canopy set to 2 m for each pixel, u* is the friction velocity (m/s), and k is the von Karman constant (0.4).

$$u^* = \frac{u(z)k}{\ln(\frac{z - d}{z_m})} \tag{13}$$

Surfaces of wind-velocity were generated by interpolating climate-station recorded wind velocities. IDW method was used to interpolate wind velocities recorded 2 m above the ground surface. Elevation differences were used as weights in the interpolation of wind velocity. The initial value for friction velocity (u*) was computed for neutral stability with data from the local meteorological station. The average height of vegetation (m) was surveyed in the site nearby the meteorological station and was used to calculate the land surface friction, Z_m. Then, Z_m for each pixel calculated by a regression equation according to the pixel NDVI value. The near-surface wind speed was converted to a value at the blending height (200-m) where the effects of the land surface roughness could be eliminated. The initial estimated values of u* were used to infer the first values of aerodynamic resistance (r_{ah}). Corrections for atmosphere stability were obtained iteratively for each pixel. This required a series of iterations to determine new values of the corrected friction velocities and the corrected aerodynamic resistances before obtaining numerical stability based on the criterion of Monin–Obukhov length.

Once sensible heat flux and the available energy (Rn-G) were determined, estimation of instantaneous ET_{ins} could be computed pixel by pixel using Equation (2). The evaporative fraction (EF) describes the partitioning of the surface energy balance as the latent heat flux/net available energy, with the net available energy being defined as the difference in net radiation and soil heat flux. In this study, we used the concept 'ETo fraction' (ETo_f), which represents the ratio of ET of each pixel to the reference ET as computed by Penman–Monteith method. ETo_f is the same as the crop coefficient, Kc; and was calculated by applied using Equation (14). Then, daily values of ET were computed using (15)

$$ETo_f = \frac{ET_{inst}}{ETo} \tag{14}$$

$$ET_{d\_Sebal} = ETo_f \times ETo_{daily} \tag{15}$$

The computation of the monthly AET involved extrapolating the SEBAL daily AET, within each month, proportional to the reference evapotranspiration where the latter was derived from standard meteorological measurements. The procedure involved determining the cumulative reference evapotranspiration between successive satellite images before computing the ratio, (K_m), of the cumulative reference evapotranspiration to the average potential ET over the period. The monthly ET, (AET_m), was then computed as follows:

$$AET_m = \sum_{i=1}^{i=n} (ET_{sebal})_i (K_m)_i \tag{16}$$

RESULTS AND DISCUSSION

Developing LC and reference evapotranspiration

A Landsat 5/7 TM/ETM image was obtained in the year 2013 from the King Abdul-Aziz City for Science and Technology. This image was incorporated with collected data from the specified region, and ultimately utilized in categorizing LC. ERDAS Imagine software used for mosaic the collected satellite images. Geometric corrections were made using an already rectified SPOT-5 '2.5 m PSM' satellite image of 06/03/2000. Iso Cluster unsupervised classification and Maximum likelihood classification method were used for the unsupervised and supervised classification. Training samples collected during field survey to create spectral signatures for the supervised classification to identify what the cluster represents. The LC map was classified into six main classes: Irrigated cropland, shrubland, sparse vegetation, built up areas, bare soil and water bodies. The extent of the LC distribution in 2013 is presented in Figure 3. The areal extent of each class and its LC are presented in Table 1. The Eastern Province is the largest province of the KSA and it occupy 24.1% of its total area. Results revealed that bare soil represents the largest portion of the area (99.45%), and only 0.37% of the total area are 'Irrigated cropland'. While, water bodies, sparse vegetation and shrubland represent 0.023%, 0.037% and 0.0127% of the total area, respectively. Built-up area accounts for about 494 km^2 or 0.1% of the total province area (Table 1).

In the present study, various meteorological data, including normal maximum temperature, minimum temperature, sunshine hours, relative humidity, wind speed and

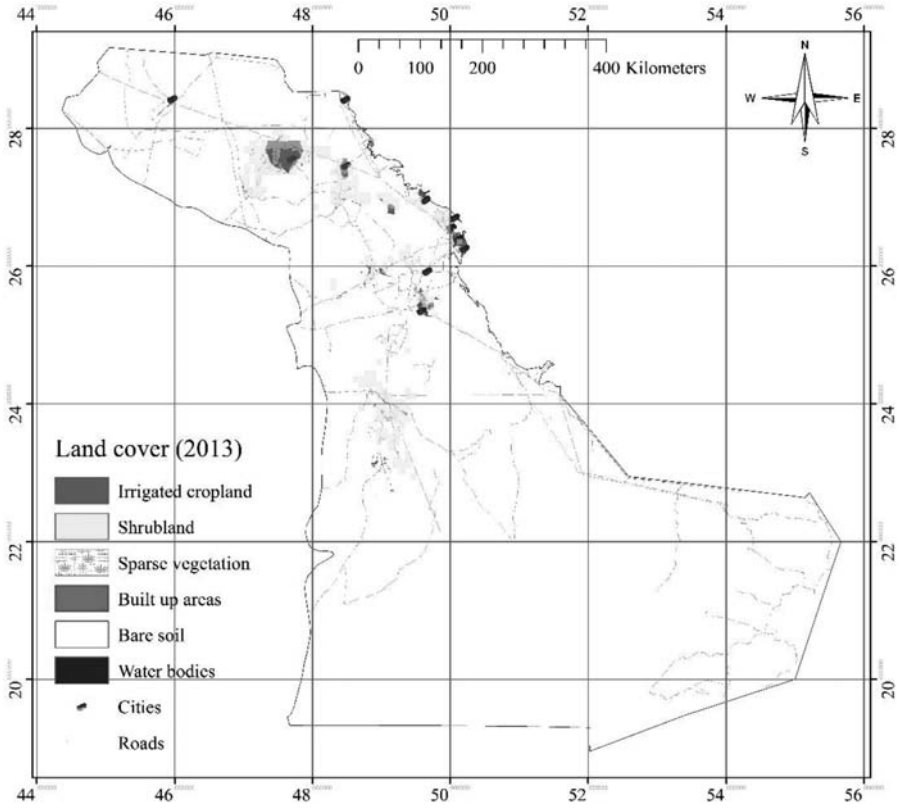

Q6 **Figure 3** | LC map of the study area.

Table 1 | Areal distribution of different LC classes

LC class	Area (%)	Area (Km^2)
Irrigated cropland	0.37	1,910
Shrubland	0.0127	66
Sparse vegetation	0.037	191.8
Built up areas	0.1	494
Bare areas	99.45	515,517
Water bodies	0.023	121.2

rainfall has been obtained from meteorological department, Ministry of Agriculture and Ministry of Water and Electricity. The FAO Penman–Monteith method was employed to model the spatial distribution of ET_o in the region. The IDW interpolation function was used to interpolate each month, with the result being twelve separate maps of mean monthly ET_o (mm/day). The monthly distribution of ET_o showed a gradual increase from January–July. On the other hand, there was a subsequent decline in monthly ET_o values from August to December (Figure 4). The lowest values were in January, where ET_o ranged from 2.46 to 3.56 mm/day in the study area. The highest values were observed in July, where ET_o ranged from 6.67 to 12 mm/day. From March–October, ET_o is found to be maximum in the Northern plains, Hafar Al-Batin, the central coastal lowlands, and the southern coastal lowlands. From December to February there is a shift of maximum ET_o towards The Empty Quarter which occupies more than half of the province and the Eastern Province borders on land with Iraq, Kuwait, Oman, Qatar, and the United Arab Emirates. This may be due to the seasonal variation in the relative humidity and wind velocity in the study area. Mean annual ET_o (1992–2013) ranged from 2,060 to 2,530 mm/yr. The spatial distributions of annual ET_o are shown in Figure 5, which reflects a combined effect of all climatological factors. The lowest annual ET_o values are located in the Empty Quarter and the Eastern Province borders with Iraq, Kuwait, Oman, Qatar, and the United Arab Emirates (2,060–2,340 mm/yr). The maximum values of ET_o

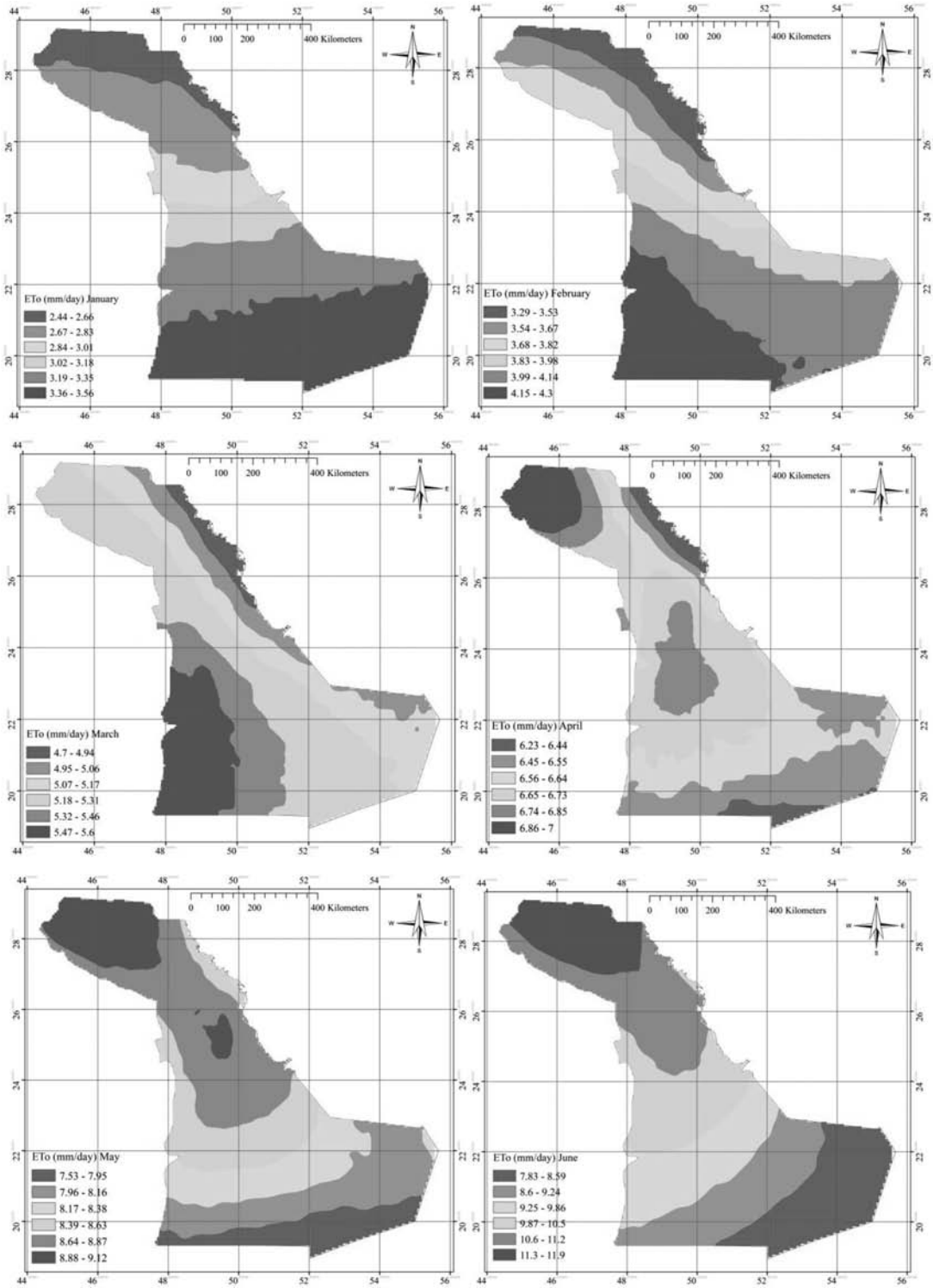

Figure 4 | Spatial distribution of monthly reference evapotranspiration (mm/day).

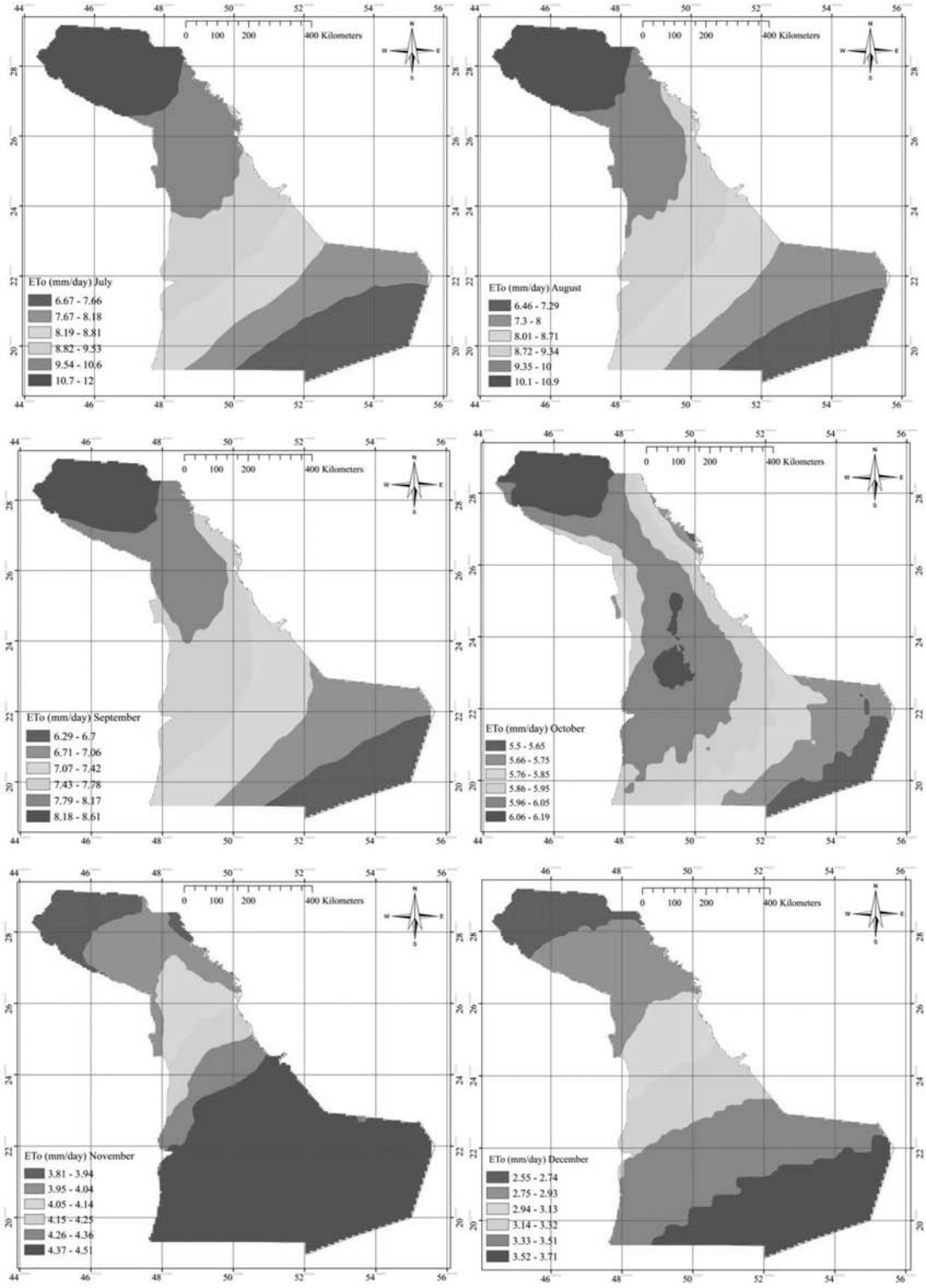

Figure 4 | continued

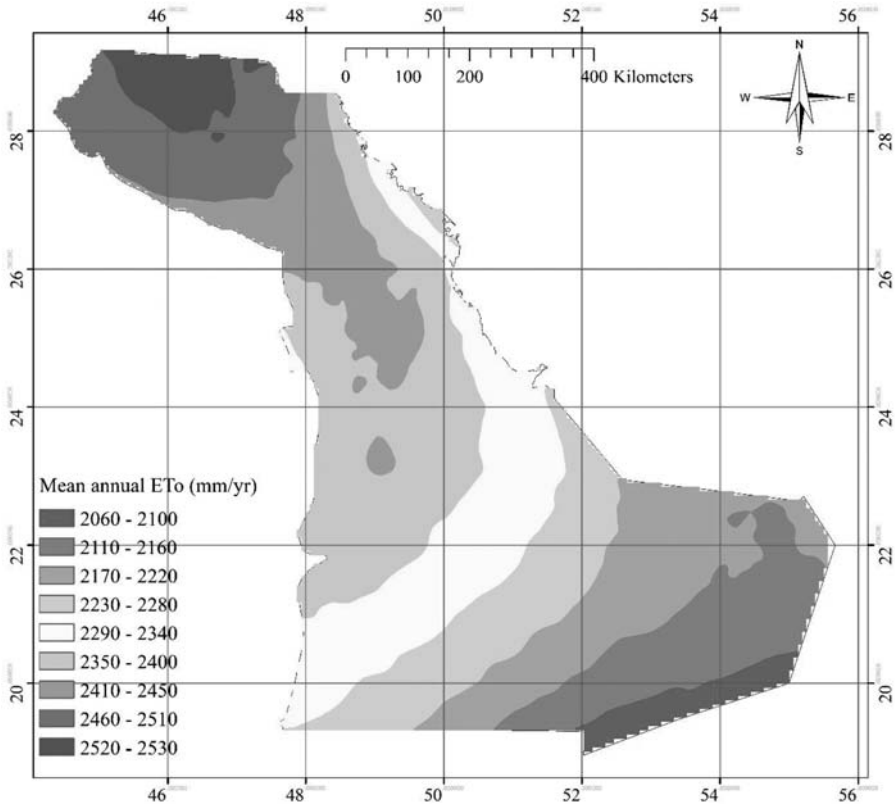

Q8 **Figure 5** | Spatial distribution of mean annual reference evapotranspiration.

rates are observed mainly over the Northern plains, Hafar Al-Batin, the central coastal lowlands, and the southern coastal lowlands (2,350–2,530 mm/yr).

Spatial–temporal distribution of AET

Figure 6 shows average monthly AET of different land uses. The highest monthly values were in April (5.22–30 mm/day. The monthly distribution of AET showed a gradual increase from January–April. In January, daily AET ranged from 0–9.18 mm/day, in February, AET ranged from 1.6–14 mm/day, in March, daily AET ranged from 3.7–26 mm/day, while the highest observed value in April ranged from 5.2–30 mm/day. On the other hand, there was a subsequent decline in daily AET values from May to December. In May daily AET ranged from 3.63–27.6 mm/day, while June daily values varied from 2.1–13.7 mm/day, and July and August daily AET ranged from 0.8–7.12 mm/day and 0.59–4.5 mm/day, respectively. The decline in daily AET values is clearly seen September to December where the daily AET range dropped from '0.59–4.5' mm/day in August to 0–2.53 mm/day in October. There was a slight increase to (0–4.28 mm/day) in November and (0–7.53) December. Nevertheless, this increase is only in irrigated cropland. In general, water consumption of various land use/cover classes shows similar seasonal dynamic trends throughout the years. The value of AET started to rise rapidly in February, reached peak values in April, and then declined to the lowest levels in September and October with a slight increase in November and December. The maximum monthly AET values in the study area were observed for irrigated cropland in the Northern plains, Hafar Al-Batin, the central coastal lowlands, and the southern coastal lowlands during the twelve months of the year. While the lowest values were observed in the Empty Quarter and the Eastern Province borders on land with Iraq, Kuwait, Oman, Qatar, and the United Arab Emirates. The actual monthly ET for all land uses follows the monthly rainfall pattern in the study area, as areas with high monthly and annual rainfall rate have high AET. This is clearly seen in the Empty

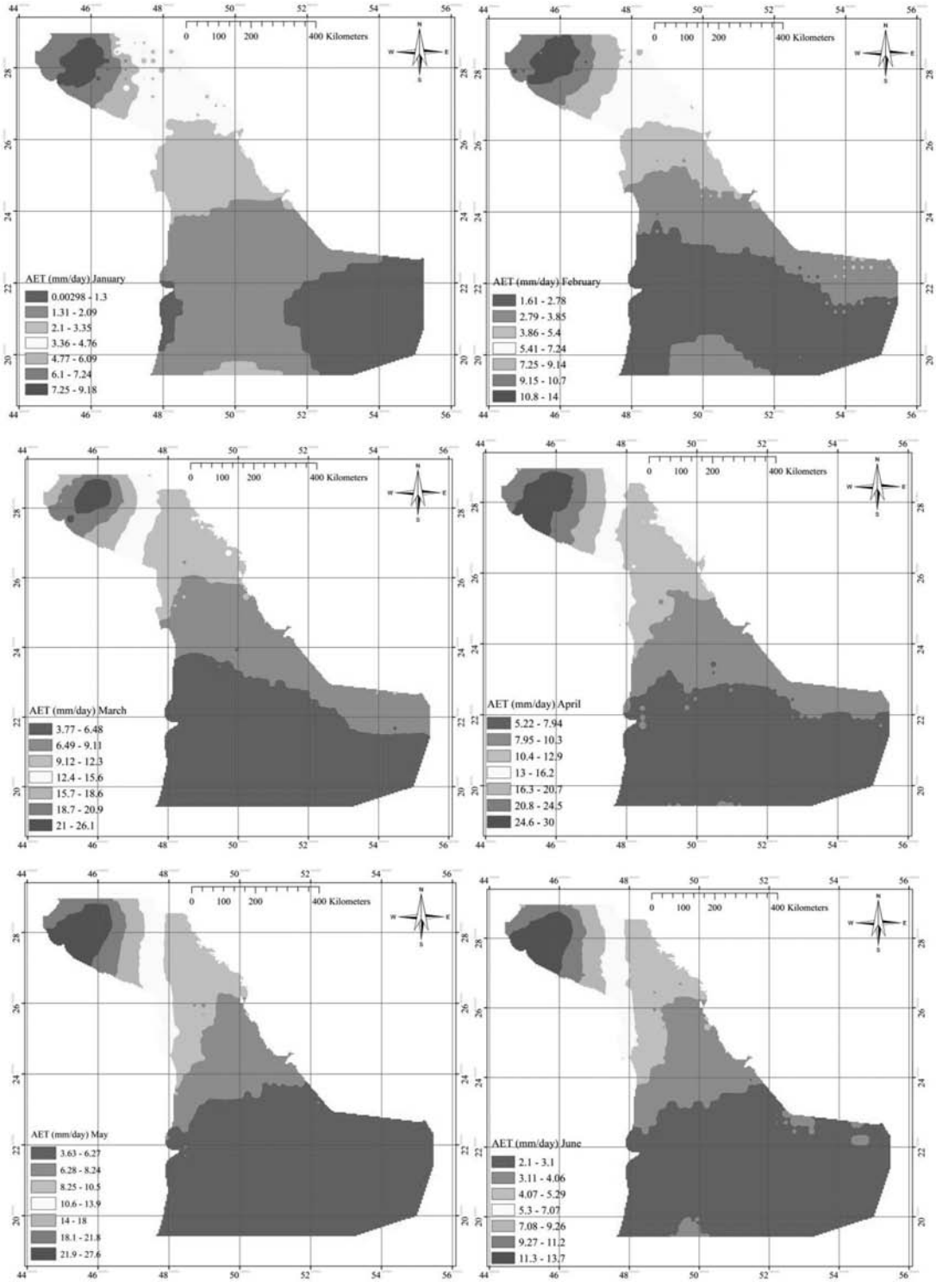

Figure 6 | Spatial distribution of average monthly AET (1992–2013).

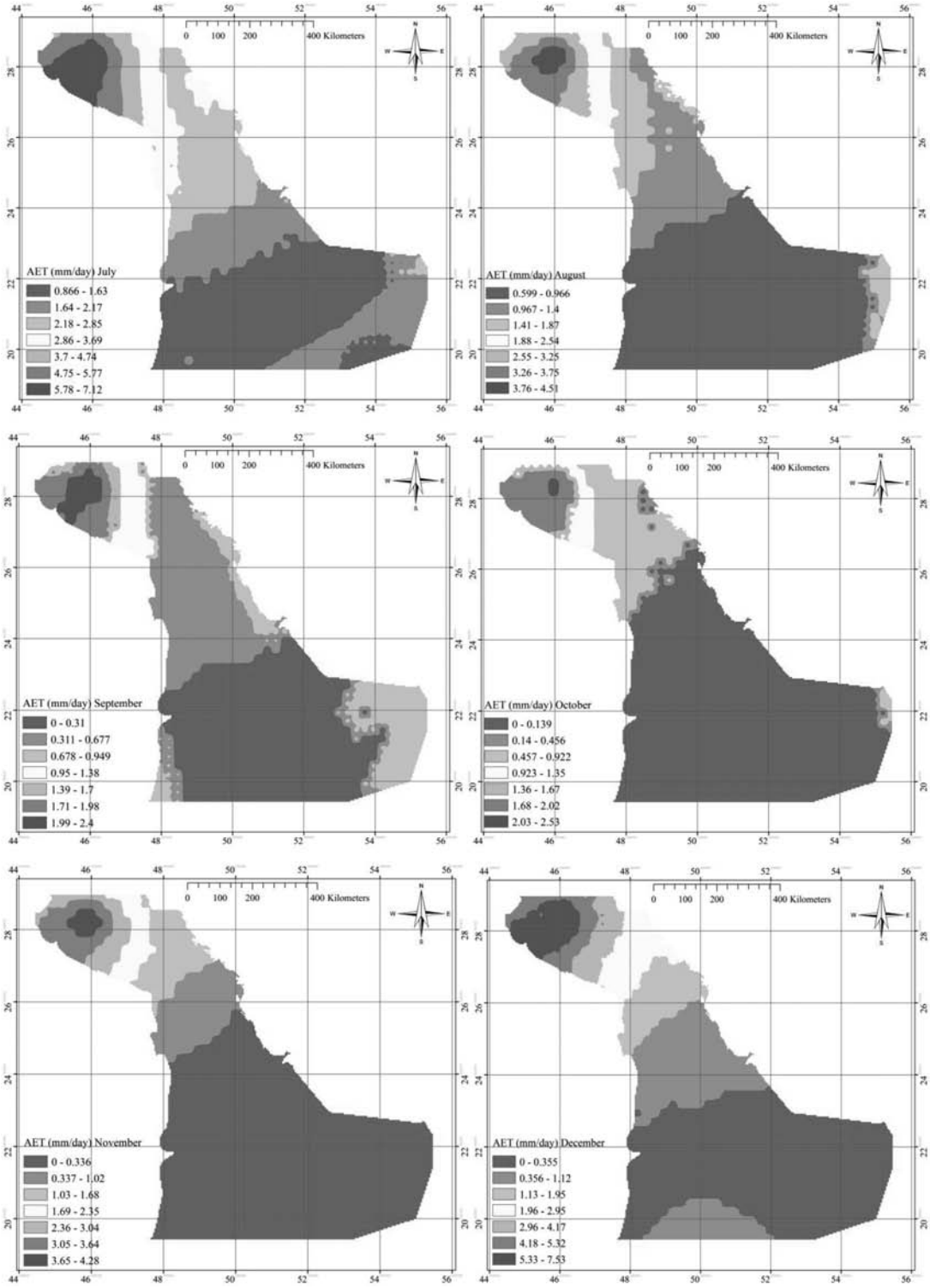

Figure 6 | continued

Quarter which receive annual rainfall less than 30 mm/yr, while the Northern plains, Hafar Al-Batin, the central coastal lowlands, and the southern coastal lowlands receive means annual rainfall range from around 113–275 mm/yr. This in good agreement with Kongo *et al.* (2011) who found that the actual monthly ET for all land uses follows the monthly rainfall pattern.

The modelled average annual AET by SEBAL model is presented in Figure 7. The spatial distribution of annual AET show low values in in the Empty Quarter (231–438 mm/yr), moderate values in the Eastern Province borders on land with Iraq, Kuwait, Oman, Qatar, and the United Arab Emirates (439–731 mm/yr). While it show very high AET values for irrigated cropland in the Northern plains, Hafar Al-Batin, the central coastal lowlands, and the southern coastal lowlands, where annual AET ranged from 732–1,790 mm/yr, representing the majority of the study area agricultural land. Figure 7 shows that built up areas and bare soil present low values of AET, while irrigated cropland show the highest values. In general, AET rates for irrigated cropland are much higher than for other land uses. Shrubland and sparse vegetation are the next highest, with water bodies slightly lower, and very low AET rates from built up areas and bare soil. This is in good agreement with Dunn & Mackay (1995) who found that irrigated cropland transpire at a slightly higher level than other vegetation, as they maintain a canopy cover throughout the year.

Estimating consumptive water use for agriculture in Saudi Arabia has always been a challenge for farmers, water managers, researchers and government agencies. Quantification of consumptive use allows for more informed water use practices, consistent measures of the allocation among stakeholders, and improved planning. Daily and annual water consumption for different land use and cover classes were computed. A summary of the values obtained for each land use and cover types are given in Table 2. The evaporative behaviour or consumptive water use of the different land use and cover types in the study area as inferred by SEBAL model indicate that irrigated cropland which occupies 0.37% of the study area have an average daily AET

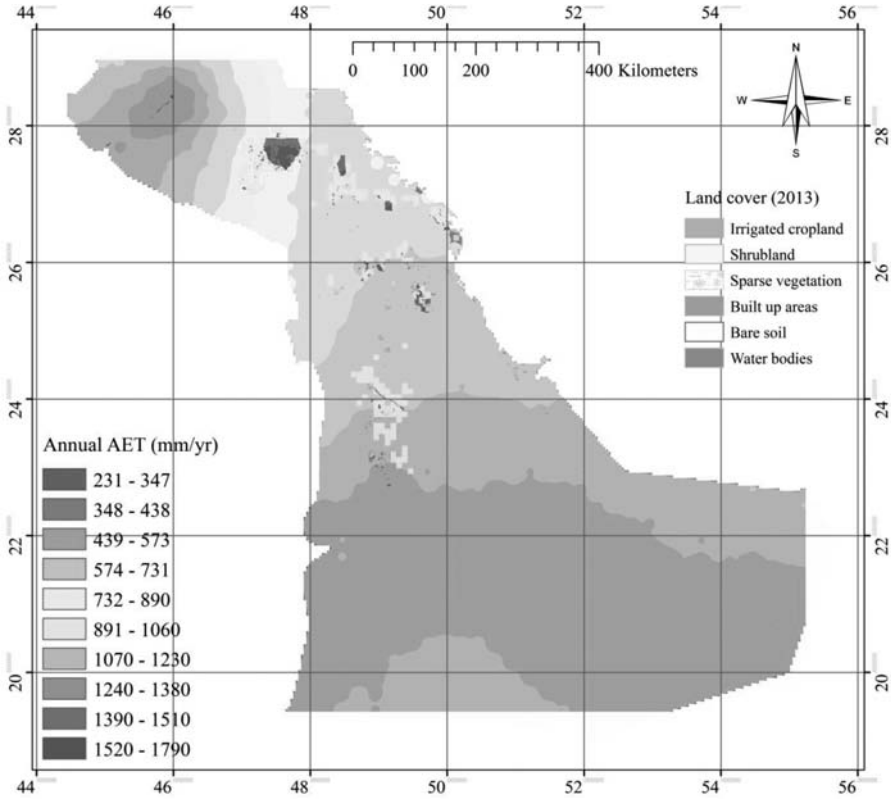

Q10 **Figure 7** | Estimated mean annual AET.

Table 2 | Monthly and annual AET of different land use and cover classes

LC class	Jan.	Feb.	Mar.	Apr.	May	June	July	Aug.	Sept.	Oct.	Nov.	Dec.	Mean annual AET AET (mm/season)
	AET (mm/day)												
Irrigated cropland	9.2	14	26.1	30	27.6	13.7	7.1	4.5	2.4	2.5	4.3	7.5	1,786.9
Shrubland	4.5	6.7	12.1	13.6	9.5	4.9	3	1.6	0.7	0.7	0.9	1.8	704
Sparse vegetation	4.8	7.4	12.5	14.3	10.3	5.2	3.4	2	0.8	0.8	1.5	2.7	760.8
Built up areas	2.37	5.79	7.92	9.4	9.2	4.49	2.8	1.47	1.1	0.9	0.86	1.5	469
Bare soil	3.6	3.94	6.72	12.8	7.63	3.94	2.25	1.17	0.5	0.6	0.5	1	608
Water bodies	4.8	7.4	12.3	14.3	9.8	5.1	3.4	2	0.7	0.8	1.5	2.6	660.8

ranges from 9.2 mm/day in January to its peak in April (30 mm/day) and drop to 7.5 mm/day in December. Mean annual water consumption by irrigated cropland is relatively very high and it's about 1,786.9 mm/yr. While, water bodies, which covers 0.023% (121.2 km^2) of the study area, also had relatively high mean AET (660.8 mm/yr). However, it covers only a limited area. Evaporative behaviour in the largest continuous sand sheet of the world has a similar trend and it follows monthly rainfall pattern in the area. Bare soil which represent 99.45% of the total area had a low evaporative behaviour, where the total annual AET is about 608 mm/day.

CONCLUSION

This study designed to model spatial and temporal distribution of reference and AET over the Eastern province of Saudi Arabia during 1992–2013 using the Surface Energy Balance based algorithm. The monthly distribution of reference evapotranspiration (ET_o) showed a gradual increase from January–July and a subsequent decline in monthly ET_o values from August to December. While, the monthly distribution of AET showed a gradual increase from January–April. On the other hand, there was a subsequent decline in daily AET values from May to December. Water consumption of various land use/cover classes show similar seasonal dynamic trends throughout the years. The maximum monthly AET values in the study area were observed for irrigated cropland in the Northern plains, Hafar Al-Batin, the central coastal lowlands, and the southern coastal lowlands during the twelve months of the year. While the lowest values were observed in the Empty Quarter and the Eastern Province borders on land with Iraq, Kuwait, Oman, Qatar, and the United Arab Emirates. The spatial distribution of annual AET show low values in in the Empty Quarter (231–438 mm/yr), moderate values in the Eastern Province borders on land with Iraq, Kuwait, Oman, Qatar, and the United Arab Emirates (439–731 mm/yr). While it shows very high AET values for irrigated cropland in the Northern plains, Hafar Al-Batin, the central coastal lowlands, and the southern coastal lowlands, where annual AET ranged from 732–1,790 mm/yr, representing the majority of the study area agricultural land. Overall, AET rates for irrigated cropland are much higher than for other land uses. Shrubland and sparse vegetation are the next highest, with water bodies slightly lower, and very low AET rates from built up areas and bare soil. Mean annual water consumption by irrigated cropland is relatively very high and it is about 1,786.9 mm/yr. While, water bodies, which covers 0.023% (121.2 km^2) of the study area, also had relatively high mean AET (660.8 mm/yr). Evaporative behaviour in the largest continuous sand sheet of the world has a similar trend and it follows monthly rainfall pattern in the area. Bare soil, which represent 99.45% of the total area, had a low evaporative behaviour, where the total annual AET is about 608 mm/yr. The successful application of SEBAL for estimating AET proves its value within the hydrological community in the study area and similar regions, and it can be used to help water managers devise sustainable water use planning and management in Saudi Arabia.

ACKNOWLEDGEMENTS

The project was financially supported by King Saud University, Vice Deanship of Research Chairs.

REFERENCES

Allen, R. G., Pereira, L. S., Raes, D. & Smith, M. 1998 Crop evapotranspiration-guidelines for computing crop water requirements-FAO Irrigation and drainage paper 56. *FAO, Rome* **300** (9), D05109.

Ayenew, T. 2003 Evapotranspiration estimation using thematic mapper spectral satellite data in the Ethiopian rift and adjacent highlands. *Journal of Hydrology* **279** (1), 83–93.

Bastiaanssen, W. G. M. 1995 *Regionalization of Surface Flux Densities and Moisture Indicators in Composite Terrain, a Remote Sensing Approach Under Clear Skies in Mediterranean Climates, Report 109*, Agricultural Department, Wageningen, The Netherlands.

Bastiaanssen, W. G. M. 2000 SEBAL-based sensible and latent heat fluxes in the irrigated Gediz Basin, Turkey. *Journal of Hydrology* **229** (1), 87–100.

Bastiaanssen, W. G. M., Menenti, M., Feddes, R. A. & Holtslag, A. A. M. 1998a A remote sensing surface energy balance algorithm for land (SEBAL): I. formulation. *Journal of Hydrology* **212**, 198–212.

Bastiaanssen, W. G. M., Pelgrum, H., Wang, J., Ma, Y., Moreno, J. F., Roerink, G. J. & Van der Wal, T. 1998b A remote sensing surface energy balance algorithm for land (SEBAL): 2. validation. *Journal of Hydrology* **212**, 213–229.

Bastiaanssen, W. G. M., Noordman, E. J. M., Pelgrum, H., Davids, G., Thoreson, B. P. & Allen, R. G. 2005 SEBAL Model with remotely sensed data to improve water-resources management under actual field conditions. *Journal of Irrigation and Drainage Engineering-ASCE* **131** (1), 85–93.

Bastiaanssen, W. G. M., Cheema, M. J. M., Immerzeel, W. W., Miltenburg, I. J. & Pelgrum, H. 2012 Surface energy balance and actual evapotranspiration of the transboundary Indus Basin estimated from satellite measurements and the ETLook model. *Water Resources Research* **48** (11).

Bausch, W. C. 1995 Remote sensing of crop coefficients for improving the irrigation scheduling of corn. *Agricultural Water Management* **27** (1), 55–68.

Boronina, A., Golubev, S. & Balderer, W. 2005 Estimation of actual evapotranspiration from an alluvial aquifer of the Kouris catchment (Cyprus) using continuous stream flow records. *Hydrological Processes* **19** (20), 4055–4068.

Chowdhury, S. & Al-Zahrani, M. 2015 Characterizing water resources and trends of sector wise water consumptions in Saudi Arabia. *Journal of King Saud University-Engineering Sciences* **27** (1), 68–82.

Department of Statistics, Information. 2008 *Statistical Yearbook*. 38–44 edn. Ministry of Economy and Planning, Kingdom of Saudi Arabia. Q2

Dunn, S. M. & Mackay, R. 1995 Spatial variation in evapotranspiration and the influence of land use on catchment hydrology. *Journal of Hydrology* **171** (1), 49–73.

Elhaddad, A., Garcia, L. A. & Chávez, J. L. 2010 Using a surface energy balance model to calculate spatially distributed actual evapotranspiration. *Journal of Irrigation and Drainage Engineering* **137** (1), 17–26.

Fu, P. & Rich, P. M. 1999 Design and implementation of the solar analyst: an ArcView extension for modeling solar radiation at landscape scales. In: *Proceedings of the Nineteenth Annual ESRI User Conference*, Chicago, pp. 1–31.

Kongo, M. V., Jewitt, G. W. P. & Lorentz, S. A. 2011 Evaporative water use of different land uses in the upper-Thukela river basin assessed from satellite imagery. *Agricultural Water Management* **98** (11), 1727–1739.

Liu, W., Hong, Y., Khan, S. I., Huang, M., Vieux, B., Caliskan, S. & Grout, T. 2010 Actual evapotranspiration estimation for different land use and land cover in urban regions using Landsat 5 data. *Journal of Applied Remote Sensing* **4** (1), 041873–041873.

Mahmoud, S. H. & Alazba, A. A. 2016 Integrated remote sensing and GIS-based approach for deciphering groundwater potential zones in the central region of Saudi Arabia. *Environmental Earth Sciences*, DOI:10.1007/s12665-015-5156-2. Q3

Menenti, M. 1984 *Physical Aspects and Determination of Evaporation in Deserts Applying Remote Sensing Techniques, Report 10 (Especial Issue)*. Institute of Land and Water Resources Management, Wageningen, The Netherlands, p. 202.

Minacapilli, M., Agnese, C., Blanda, F., Cammalleri, C., Ciraolo, G., D'Urso, G., Iovino, M., Pumo, D., Provenzano, G. & Rallo, G. 2009 Estimation of actual evapotranspiration of Mediterranean perennial crops by means of remote sensing based surface energy balance models. *Hydrology and Earth System Sciences* **13** (7), 1061–1074.

Monteith, J. L. 1965 Evaporation and environment. *In Symp. Soc. Exp. Biol.* **19**, 205–234.

Papadavid, G., Hadjimitsis, D., Toulios, L. & Michaelides, S. 2011 Mapping potatoes crop height and LAI through vegetation indices using remote sensing, in Cyprus. *Journal of Applied Remote Sensing* **5**, 053526.

Parodi, G. 1993 An Up-to-date Inventory of Remote Sensing Potentially in the Energy Balance Equation Approach for Actual Evapotranspiration Mapping. *Basic theory and Prospects (Doctoral dissertation,* Msc thesis, ITC, Enschede, The Netherlands).

Ramos, J. G., Kay, J. A., Cratchley, C. R., Casterad, M. A., Herrero, J., López, R., Martínez-Cob, A. & Domínguez, R. 2006 Crop management in a district within the Ebro River Basin using remote sensing techniques to estimate and map irrigation volumes. *WIT Transactions on Ecology and the Environment* **96**, 365–377.

Ruiz-Arias, J. A., Tovar-Pescador, J., Pozo-Vázquez, D. & Alsamamra, H. 2009 A comparative analysis of DEM-based models to estimate the solar radiation in mountainous terrain. *International Journal of Geographical Information Science* **23** (8), 1049–1076.

Sánchez, J. M., Scavone, G., Caselles, V., Valor, E., Copertino, V. A. & Telesca, V. 2008 Monitoring daily evapotranspiration at

a regional scale from Landsat-TM and ETM + data: application to the Basilicata region. *Journal of Hydrology* **351** (1), 58–70.

Senay, G. B., Budde, M., Verdin, J. P. & Melesse, A. M. 2007 A coupled remote sensing and simplified surface energy balance approach to estimate actual evapotranspiration from irrigated fields. *Sensors* **7** (6), 979–1000.

Singh, R. K., Irmak, A., Irmak, S. & Martin, D. L. 2008 Application of SEBAL model for mapping evapotranspiration and estimating surface energy fluxes in south-central Nebraska. *Journal of Irrigation and Drainage Engineering* **134** (3), 273–285.

Teixeira, A. D. C., Bastiaanssen, W. G. M., Ahmad, M. & Bos, M. G. 2009 Reviewing SEBAL input parameters for assessing evapotranspiration and water productivity for the low-middle São Francisco River basin, Bazil. Part A: calibration and validation. *Agr. Forest Meteorol.* **149**, 462–476.

Wang, J., Ma, Y., Menenti, M., Bastiaanssen, W. G. M. & Mitsuta, Y. 1995 The scaling-up of processes in the heterogeneous landscape of HEIFE with the aid of satellite remote sensing. *Journal of the Meteorological Society of Japan* **73** (6), 1234–1244.

Wang, K., Wang, P., Li, Z., Cribb, M. & Sparrow, M. 2007 A simple method to estimate actual evapotranspiration from a combination of net radiation, vegetation index, and temperature. *Journal of Geophysical Research: Atmospheres (1984–2012)*, **112** (D15).

Wanner, W., Strahler, A. H., Hu, B., Lewis, P., Muller, J. P., Li, X., Schaaf, C. L. & Barnsley, M. J. 1997 Global retrieval of bidirectional reflectance and albedo over land from EOS MODIS and MISR data: theory and algorithm. *Journal of Geophysical Research-Atmospheres* **102** (D14), 17143–17161.

Wu, X., Zhou, J., Wang, H., Li, Y. & Zhong, B. 2015 Evaluation of irrigation water use efficiency using remote sensing in the middle reach of the Heihe River, in the semi-arid Northwestern China. *Hydrological Processes* **29** (9), 2243–2257.

Zhou, L., Dickinson, R. E., Tian, Y., Zeng, X., Dai, Y., Yang, Z. L., Schaaf, C. B., Gao, F., Jin, Y., Strahler, A. & Myneni, R. B. 2003 Comparison of seasonal and spatial variations of albedos from moderate-resolution imaging spectroradiometer (MODIS) and common land model. *Journal of Geophysical Research: Atmospheres (1984–2012)*, **108** (D15).

First received 22 December 2015; accepted in revised form 20 April 2016. Available online 29 April 2016

Author Queries

Journal: Water Science & Technology: Water Supply

Manuscript: WS-EM15582R1

Q1 Papadavid (2011) has been changed to Papadavid *et al.* (2011) as per the reference list.

Q2 Department of Statistics and Information (2008) is not cited in the main text. Please confirm where it should be cited, or delete the reference.

Q3 Please update volume and page number for Mahmoud & Alazba (2016).

Q4 In supplied Figure 1 is not sufficient print quality. Please resupply as a high resolution file (300 dpi or above) with sharp lines and text.

Q5 In supplied Figure 2 is not sufficient print quality. Please resupply as a high resolution file (300 dpi or above) with sharp lines and text.

Q6 In supplied Figure 3 is not sufficient print quality. Please resupply as a high resolution file (300 dpi or above) with sharp lines and text.

Q7 In supplied Figure 4 is not sufficient print quality. Please resupply as a high resolution file (300 dpi or above) with sharp lines and text.

Q8 In supplied Figure 5 is not sufficient print quality. Please resupply as a high resolution file (300 dpi or above) with sharp lines and text.

Q9 In supplied Figure 6 is not sufficient print quality. Please resupply as a high resolution file (300 dpi or above) with sharp lines and text.

Q10 In supplied Figure 7 is not sufficient print quality. Please resupply as a high resolution file (300 dpi or above) with sharp lines and text.